International Tables for Crystallography (2006). Vol. C, Chapter 2.7, pp. 113–123.

2.7. Topography

BY A. R. LANG

2.7.1. Principles

The term diffraction topography covers techniques in which images of crystals are recorded by Bragg-diffracted rays issuing from them. It can be arranged at will for these rays to produce an image of a surface bounding the crystal, or of a thin slice cutting through the crystal, or of the projection of a selected volume of the crystal. The majority of present-day topographic techniques aim for as high a spatial resolution as possible in their point-by-point recording of intensity in the diffracted rays. In principle, any position-sensitive detector with adequate spatial resolution could be employed for recording the image. Photographic emulsions are most widely used in practice. In the following accounts of the various diffraction geometries developed for topographic experiments, the term 'film' will be used to stand for photographic emulsion coated on film or on glass plate, or for any other position-sensitive detector, either integrating or capable of real-time viewing, that could serve instead of photographic emulsion. (Position-sensitive detectors, TV cameras, and storage phosphors are described in Sections 7.1.6, 7.1.7, and 7.1.8.) All diffraction geometries described with reference to an X-ray source could in principle be used with neutron radiation of comparable wavelength (see Chapter 4.4).

Two factors, often largely independent and experimentally distinguishable, determine the intensity that reaches each point on the topograph image. The first is simply whether or not the corresponding point in the specimen is oriented so that some rays within the incident beam impinging upon it can satisfy the Bragg condition. The intensity of the Bragg-reflected rays will range between maximum and minimum values depending upon how well that condition is satisfied. The consequent intensity variation from point to point on the image is called *orientation contrast*, and it can be analysed to provide a map of lattice misorientations in the specimen. The sensitivity of misorientation measurement is controllable over a wide range by appropriate choice of diffraction geometry, as will be explained below. The second factor determining the diffracted intensity is the lattice perfection of the crystal. In this case, physical factors such as X-ray wavelength, specimen absorption, and structure factor of the active Bragg reflection fix the range within which the diffracted intensity can lie. One limit corresponds to the case of the *ideally perfect crystal*. This is a well defined entity, and its diffraction behaviour is well understood [see *IT* B (1996, Part 5)]. The other limit is that of the *ideally imperfect crystal*, a less precisely defined entity, but which, for practical purposes, may be taken as a crystal exhibiting negligible primary and secondary extinction. The magnitude, and sometimes also the sign, of the difference in intensity recorded from volume elements of ideally perfect as opposed to ideally imperfect crystals is to a large degree controllable by the choice of experimental parameters (in particular by choice of wavelength). Contrast on the topograph image arising from point-to-point differences in lattice perfection of the specimen crystal was called *extinction contrast* in earlier X-ray topographic work, but is now more usually called *diffraction contrast* to conform with terminology used in transmission electron microscopic observations of lattice defects, experiments which have many analogies with the X-ray case.

Figs. 2.7.1.1 and 2.7.1.2, respectively, show in plan view the simplest arrangements for taking a *reflection* topograph and a *transmission* topograph. The source of X-rays is shown as being point-like at S. If its wavelength spread is large then the Bragg condition may be satisfied over the whole length CD for Bragg planes oriented parallel to BB', and an image of CD will be formed on F by the Bragg-diffracted rays falling on it. The specimen is mounted on a rotatable axis (the ω axis) perpendicular to the plane of the drawing, which represents the median plane of incidence, in order that the angle of incidence on the planes BB' can be varied. The specimen is usually adjusted so that the diffraction vector, **h**, of the Bragg reflection of principal interest is perpendicular to the ω axis. Let the mean source-to-specimen and specimen-to-film distances be a and b, respectively. Suppose the source S is extended a distance s in the axial direction (*i.e.* perpendicular to the plane of incidence). Then diffracted rays from any point on CD will be spread on F over a distance $s(b/a)$ in the axial direction. This is the simple expression for the axial resolution of the topograph given by ray optics. Transmission topographs have the value of showing defects within the interior of specimens, which may be optically opaque, but are in practice limited to a specimen thickness, t, such that μt is less than a few units (μ being the normal linear absorption coefficient) unless the specimen structure and the perfection are such as to allow strong anomalous transmission [the Borrmann effect, see *IT* B (1996, Part 5)]. If a reflection topograph specimen is a nearly perfect crystal then the volume of crystal contributing to the image is restricted to a depth below the surface given approximately by the X-ray extinction distance, ξ_h, of the active Bragg reflection, which may be only a few micrometres, rather than the penetration distance, μ^{-1}, of the radiation used.

Besides the ratio b/a, other important experimental parameters are the degree of collimation of the incident beam and its wavelength spread. The manner in which X-ray topographs exhibit *orientation contrast* and *diffraction contrast* under different choices of these parameters is illustrated schematically in Fig. 2.7.1.3. There, (*a*) represents a hypothetical specimen consisting of a matrix of perfect crystal C in which are embedded two islands A and B whose lattices differ from C in the following respects. A has the same mean orientation as C but is a region of

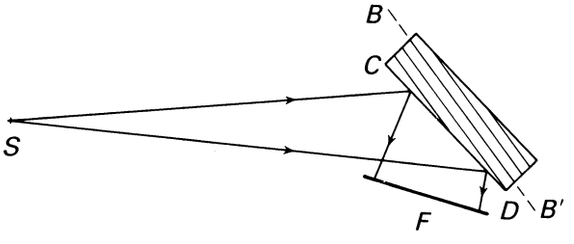

Fig. 2.7.1.1. Surface reflection topography with a point source of diverging continuous radiation.

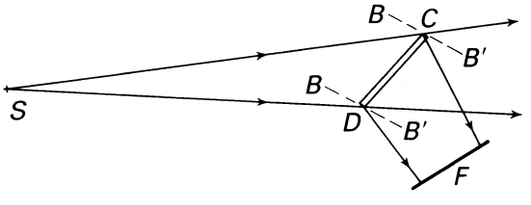

Fig. 2.7.1.2. Transmission topography with a point source of diverging continuous radiation.

high imperfection. (In reflection topographs, imperfect regions will always produce stronger *integrated* reflections than perfect regions and will also do so in transmission topographs under low-absorption conditions.) The island B is assumed to be as perfect as C, but is slightly misoriented with respect to C. The topograph images sketched in (b)–(e) could represent either reflection topographs or transmission topographs from a specimen thin compared with the dimension CD in Fig. 2.7.1.2. [Possible distortion of the images relative to the shape of (a) is neglected: this matter is considered later.] First, suppose that continuous radiation is emitted from the source S. If the ratio b/a is quite small, the topograph image will resemble (b). The island A is detected by diffraction contrast whereas island B will not show any area contrast since by assumption the incident radiation contains wavelengths enabling B to satisfy the Bragg condition just as well as C. The low-angle B–C boundary may show up, however, since it contains dislocations that will produce diffraction contrast and might be individually resolvable with a high-resolution topographic technique. Orientation contrast of B becomes manifest when b is increased, and measurement of the misorientation is then possible from the displacement of the image of B [as shown in (c)] consequent upon the different direction of Bragg-reflected rays issuing from it compared with those from C.

Next, suppose that S emits a limited range of wavelengths, *e.g.* characteristic $K\alpha$ radiation, and let the incident beam be collimated to have an angular spread in the plane of incidence that is smaller than the component in that plane of the misorientation between B and C, but larger than the angular range of reflection of C or A. Then, if the specimen is rotated about the ω axis so that A and C satisfy the Bragg condition, B will not do so and the topograph will resemble (d). [Island A shows up in (d) by diffraction contrast, as in (b).]. Appropriate rotation of the specimen will bring B into the Bragg-reflecting orientation, but will eliminate reflection from A and C, as shown in (e). The images (d) and (e) will not undergo significant change with variation in the ratio b/a, except for loss of resolution as b/a increases. The sensitivity of misorientation measurement will increase as the angular and wavelength spread of the incident beam are reduced, but when the angular range of a monochromatic incident beam is lowered to a value comparable with the angular range of reflection of the perfect crystal (generally only a few seconds of arc), it will not be possible with one angular setting alone to obtain an image that will distinguish between diffraction contrast and orientation contrast in the clear way shown in (d). The distinction will require comparison of a series of topographs obtained during a step-wise sweep of the angular range of reflection by the specimen. This is the procedure adopted in double-crystal or multicrystal topography, as described in Sections 2.7.3 and Subsection 2.7.4.2.

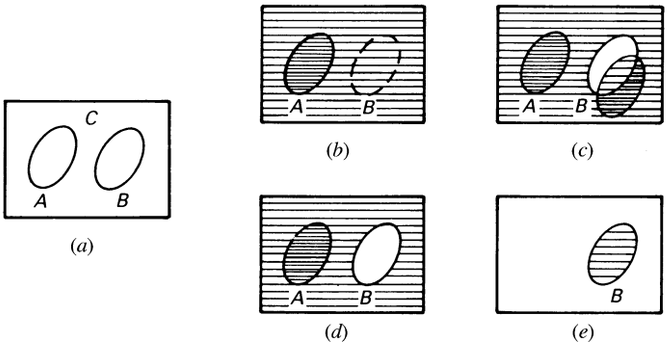

Fig. 2.7.1.3. Differentiation between orientation contrast and diffraction contrast in types of topograph images, (b)–(e), of a crystal surface (a).

Details concerning diverse variants in diffraction geometry used in X-ray topographic experiments, treatments of the diffraction contrast theory underlying X-ray topographic imaging of lattice defects, and listings of applications of X-ray topography can be found in reviews and monographs of which a selection follows. All aspects of X-ray topography are covered in the survey edited by Tanner & Bowen (1980). Armstrong & Wu (1973), Tanner (1976), and Lang (1978) describe experimental techniques and review their applications. The dynamical-diffraction theoretical basis of X-ray topography is emphasized by Authier (1970, 1977). Kato (1974) and Pinsker (1978) deal comprehensively with X-ray dynamical diffraction theory, which is also the topic of Part 5 of *IT* B (1996). Introductions to this theory have been presented by Batterman & Cole (1964), Hart (1971), and Hildebrandt (1982), the latter two being especially relevant to X-ray topography.

2.7.2. Single-crystal techniques

2.7.2.1. *Reflection topographs*

Combining the simple diffraction geometry of Fig. 2.7.1.1 with a laboratory microfocus source of continuous radiation offers a simple yet sensitive technique for mapping misorientation textures of large single crystals (Schulz, 1954). One laboratory X-ray source much used produces an apparent size of S 30 μm in the axial direction and 3 μm in the plane of incidence. Smaller source sizes can be achieved with X-ray tubes employing magnetic focusing of the electron beam. Then b/a ratios between $\frac{1}{2}$ and 1 can be adopted without serious loss of geometric resolution, and, with $a = 0.3$ m typically, misorientation angles of $10''$ can be measured on images of the type (c) in Fig. 2.7.1.3. The technique is most informative when the crystal is divided into well defined subgrains separated by low-angle boundaries, as is often the case with annealed melt-grown crystals. On the other hand, when continuous lattice curvature is present, as is usually the case in all but the simplest cases of plastic deformation, it is difficult to separate the relative contributions of orientation contrast and diffraction contrast on topographs taken by this method. In principle, the separation could be effected by recording a series of exposures with a wide range of values of b, and it becomes practicable to do so when exposures can be brief, as they can be with synchrotron-radiation sources (see Section 2.7.4.).

For easier separation of orientation contrast and diffraction contrast, and for quicker exposures with conventional X-ray sources, collimated characteristic radiation is used, as in the Berg–Barrett method. Barrett (1945) improved an arrangement earlier described by Berg (1931) by using fine-grain photographic emulsion and by minimizing the ratio b/a, and achieved high topographic resolution (~ 1 μm). The method was further developed by Newkirk (1958, 1959). A typical Berg–Barrett arrangement is sketched in Fig. 2.7.2.1. Usually, the source S is

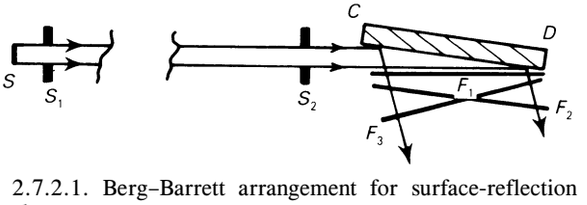

Fig. 2.7.2.1. Berg–Barrett arrangement for surface-reflection topographs.

the focal spot of a standard X-ray tube, giving an apparent source 1 mm square perpendicular to the incident beam. The openings of the slits S_1 and S_2 are also 1 mm in the plane of incidence, and the distance S_1–S_2 (which may be identified with the distance a) is typically 0.3 m. The specimen is oriented so as to Bragg reflect asymmetrically, as shown. Softer radiations, *e.g.* Cu $K\alpha$, Co $K\alpha$ or Cr $K\alpha$, are employed and higher-angle Bragg reflections are chosen ($2\theta_B \simeq 90^\circ$ is most convenient). Fig. 2.7.2.1 indicates three possible film orientations, F_1–F_3. (These possibilities apply in most X-ray topographic arrangements.) Choice of orientation is made from the following considerations. If minimum distance b is required over the whole length CD, then position F_1 is most appropriate. If a geometrically undistorted image of CD is needed, then position F_2, in which the film plane is parallel to the specimen surface, satisfies this condition. If a thick emulsion is used, it should receive X-rays at normal incidence, and be in orientation F_3. If high-resolution spectroscopic photographic plates are used, in which the emulsion thickness is $\sim 1\,\mu$m only, then considerable obliquity of incidence of the X-rays is tolerable. But these plates have low X-ray absorption efficiency. Nuclear emulsions (particularly Ilford type L4) are much used in X-ray topographic work. Ilford L4 is a high-density emulsion (halide weight fraction 83%) and hence has high X-ray stopping power. The usual minimum emulsion thickness is 25 μm. Such emulsions should be oriented not more than about 2° off perpendicularity to the X-ray beam if resolution loss due to oblique incidence is not to exceed 1 μm (with correspondingly closer limits on obliquity for thicker emulsions). With 1 mm openings of S_1 and S_2, and $a = 0.3$ m, most of the irradiated area of CD will receive an angular range of illumination sufficient to allow both components of the $K\alpha$ doublet to Bragg reflect. In these circumstances, the distance b must be everywhere less than 1–2 mm if image spreading due to superimposition of the α_1 and α_2 images is not to exceed a few micrometres. In order to eliminate this major cause of resolution loss (and, incidentally, gain sensitivity in misorientation measurements), the apertures S_1 and S_2 should be narrowed and/or a increased so that the angular range of incidence on the specimen is less than the difference in Bragg angle of the α_1 and α_2 components for the particular radiation and Bragg angle being used. (This condition applies equally in the transmission specimen techniques, described below.). With a narrower beam, the illuminated length of CD is reduced. This disadvantage may be overcome by mounting the specimen and film together on a linear traverse mechanism so that during the exposure all the length of CD of interest is scanned. In this way, surface-reflection X-ray topographs can be recorded for comparison with, say, etch patterns or cathodoluminescence patterns (Lang, 1974).

2.7.2.2. *Transmission topographs*

The term 'X-ray topograph' was introduced by Ramachandran (1944) who took transmission topographs of cleavage plates of diamond using essentially the arrangement shown in Fig. 2.7.1.2. (In this case, S was a 0.3 mm diameter pinhole placed in front of the window of a W-target X-ray tube so as to form a point source of diverging continuous radiation.) Ramachandran adopted a distance $a = 0.3$ m and ratio a/b of about 12, which produced images of about 25 μm geometrical resolution having the characteristics of Fig. 2.7.1.3(*b*), *i.e.* sensitive to diffraction contrast but not to orientation contrast. For each reflection under study, the film was inclined to the incident beam with that obliquity calculated to produce an undistorted image of the specimen plate. Guinier & Tennevin (1949) studied both diffraction contrast and orientation contrast in continuous-radiation transmission topograph images. Their minimum b/a ratio was set by the need to avoid overlap of Laue images of the crystal produced by different Bragg planes.

Collimated characteristic radiation is used in the methods of 'section topographs' (Lang, 1957) and 'projection topographs' (Lang, 1959*a*), the latter being sometimes called 'traverse topographs'. Fig. 2.7.2.2 explains both techniques. When taking a section topograph, the specimen CD, usually plate shaped, is stationary (disregard the double-headed arrow in the figure). The ribbon-shaped incident beam issuing from the slit P is Bragg reflected by planes normal, or not far from normal, to the major surfaces of the specimen. As drawn, the Bragg planes make an angle α with the normal to the X-ray entrance surface of the specimen, the positive sense of α being taken in the same sense as the deviation $2\theta_B$ of the Bragg-reflected rays. If the crystal is sufficiently perfect for multiple scattering to occur within it (with or without loss of coherence), then the multiply scattered rays associated with the Bragg reflection excited will fill the volume of the triangular prism whose base is ORT, the 'energy-flow triangle' or 'Borrmann triangle', contained between OT and OR whose directions are parallel to the incident wavevector, $\mathbf{K}_0$, and diffracted wavevector, $\mathbf{K}_h$, respectively. Both the $\mathbf{K}_0$ and $\mathbf{K}_h$ beams issuing from the X-ray exit surface of the crystal carry information about the lattice defects within the crystal. However, it is usual to record only the $\mathbf{K}_h$ beam. This falls on the film, F, in a strip extending normal to the plane of incidence, of height equal to the illuminated height of the specimen multiplied by the axial magnification factor $(a + b)/a$, and forms the section topograph image. The screen, Q, prevents the $\mathbf{K}_0$ beam from blackening the film but has a slot allowing the diffracted beam to fall on F. A diffraction-contrast-producing lattice defect cut by OT at I will generate supplementary rays parallel to $\mathbf{K}_h$ and will produce an identifiable image on F at I', the 'direct image' or 'kinematic image' of the defect. The depth of I within CD can be found *via* the measurement of $I'T'/R'T'$. From a series of section topographs taken with a known translation of the specimen between each topograph, a three-dimensional construction of the trajectory of defect I (*e.g.* a dislocation line) within the crystal can be built up. To obtain good definition of the spatial width of the ribbon incident beam cutting the crystal, the distance between P and the crystal is kept small. The minimum practicable opening of P is about 10 μm. If diffraction is occurring from planes perpendicular to the X-ray entrance surface of the specimen, *i.e. symmetrical Laue case* diffraction, the width $R'T'$ of the section topograph image is simply $2t \sin\theta_B$, t being the specimen thickness, and neglecting the contribution from the

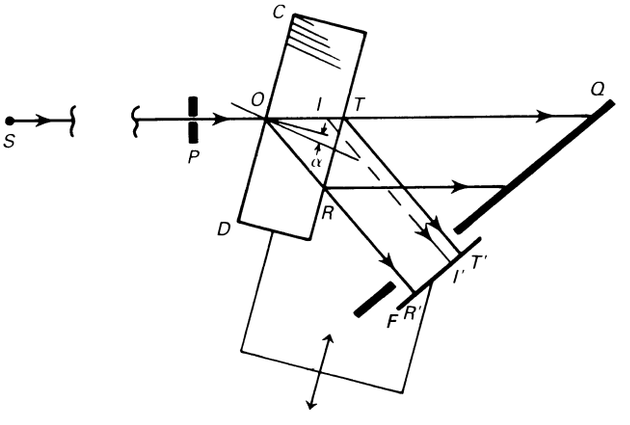

Fig. 2.7.2.2. Arrangements for section topographs and projection topographs.

width of the ribbon incident beam. With asymmetric transmission, as drawn in the figure, $R'T' = t\sec(\theta_B - \alpha)\sin 2\theta_B$. The distance b is made as small as is permitted by the specimen shape and the need to separate the emerging $\mathbf{K}_0$ and $\mathbf{K}_h$ beams. Suppose b is 10 mm. Then, with a source S having axial extension 100 μm, the distance $a = SP$ should be not less than 0.5 m in order to keep the geometrical resolution in the axial direction better than 2 μm, and should be correspondingly longer with larger source sizes.

To take a projection topograph, the specimen CD and the cassette holding the film F are together mounted on an accurate linear traversing mechanism that oscillates back and forth during the exposure so that the whole area of interest in the specimen is scanned by the ribbon beam from P. The screen Q is stationary. If the specimen is plate shaped, the best traverse direction to choose is that parallel to the plate, as indicated by the double-headed arrow, for then the diffracted beam will have minimum side-to-side oscillation during the traverse oscillation, the opening of Q can be held to a minimum, and thereby unwanted scattering reaching F kept low. The projection topograph image is an orthographic projection parallel to $\mathbf{K}_h$ of the crystal volume and its content of diffraction-contrast-producing lattice defects. If the specimen is plate-like, of length L in the plane of incidence, then, with F normal to $\mathbf{K}_h$, the magnification of the topograph image in the direction parallel to the plane of incidence is $L\cos(\theta_B + \alpha)$. There will generally be a small change of axial magnification $(a + b)/a$ along L. The loss of three-dimensional information occurring through projection can be recovered by taking stereopairs of projection topographs. The first method (Lang, 1959*a*,*b*) used hkl, $\bar{h}\bar{k}\bar{l}$ pairs of topographs as stereopairs. One disadvantage of this method is that the convergence angle is fixed at $2\theta_B$, which may be unsuitably large for thick specimens. The method of Haruta (1965) obtains two views of the specimen using the same hkl reflection, by making a small rotation of the specimen about the **h** vector between the two exposures, and has the advantage that this rotation, and hence the stereoscopic sensitivity, can be chosen at will. When taking projection topographs, the slit P can be wider than the narrow opening needed for high-resolution section topographs, but not so wide as to cause unwanted $K\alpha_2$ reflection to occur. Best use of the X-ray source is made when the width of P is the same as or somewhat greater than S.

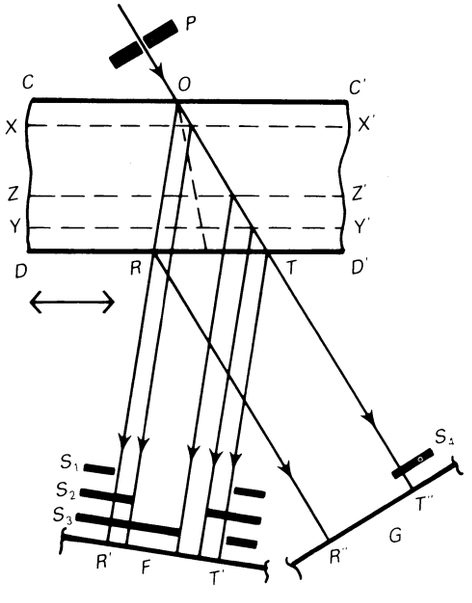

Fig. 2.7.2.3. Arrangements for limited projection topographs and direct-beam topographs.

In certain investigations, the methods of $\mathbf{K}_h$-beam 'limited projection topographs' (Lang, 1963) and of $\mathbf{K}_0$-beam section topographs and projection topographs are useful; Fig. 2.7.2.3 shows the arrangement of screens and diffracted-beam slits then adopted. The limited projection topograph technique can be employed with a plate-shaped specimen $CDD'C'$, as in the following examples. Suppose the surface of the plate contains abrasion damage that cannot be removed but that causes diffraction contrast obscuring the images of interior defects in the crystal. The diffracted-beam slit (equivalent to the opening in Q shown in Fig. 2.7.2.2), which is opened to the setting S_1 for a standard projection topograph, may now be closed down to setting S_2 so as to cut into the RR' and TT' edges of the $\mathbf{K}_h$ beam, and thereby prevent direct images of near-surface defects located between CC' and XX', and between YY' and DD', from reaching F. As another example, it may be desired to receive direct images from a specimen surface and a limited depth below it only (*e.g.* when correlating surface etch pits with dislocation outcrops). Then, setting S_3 of the diffracted-beam slit is adopted and only the direct images from defects lying between depth ZZ' and the surface DD' reach F.

To record the $\mathbf{K}_0$ beam image, either in a section topograph or a projection topograph, some interception of the $\mathbf{K}_0$ beam on the OTT'' side is needed to avoid intense blackening of the film G by radiation coming from the source, which will generally contain much energy in wavelengths other than those undergoing Bragg diffraction by the crystal. Screen S_4, critically adjusted, performs the required interception. Recording both $\mathbf{K}_0$-beam and $\mathbf{K}_h$-beam images is valuable in some studies of dynamical diffraction phenomena, such as the 'first-fringe contrast' in stacking-fault fringe patterns (Jiang & Lang, 1983). Such recording can be done simultaneously, on separate films, normal to $\mathbf{K}_0$ and $\mathbf{K}_h$, respectively, when $2\theta_B$ is sufficiently large.

When collimated characteristic radiation is used, recording projection topographs of reasonably uniform density becomes difficult when the specimen is bent. To keep the ω axis oriented at the peak of the Bragg reflection while the specimen is scanned, several devices for 'Bragg-angle control' have been designed, for example the servo system of Van Mellaert & Schwuttke (1972). The signal is taken from a detector registering the Bragg reflection through the film F, but this precludes use of glass-backed emulsions if X-ray wavelengths such as that of Cu K and softer are used. An alternative approach with thin, large-area transmission specimens is to revert to the geometry of Fig. 2.7.1.2 and deliberately elastically bend the crystal to such radius as will enable its whole length to Bragg diffract a single wavelength diverging from S, similar to a Cauchois focusing transmission monochromator (Wallace & Ward, 1975). No specimen traversing is then needed, but b cannot be made small if the wide $\mathbf{K}_0$ and $\mathbf{K}_h$ beams are to be spatially separated in the plane of F.

Quite simple experimental arrangements can be adopted for taking transmission topographs under high-absorption conditions, when only anomalously transmitted radiation can pass through the crystal. The technique has mainly been used in symmetrical transmission, as shown with the specimen $CC'D'D$ in Fig. 2.7.2.4. When the specimen perfection is sufficiently high for the Borrmann effect to be strongly manifested, and $\mu t > 10$, say, the energy flow transmitted within the Borrmann triangle is constricted to a narrow fan parallel to the Bragg planes, the fan opening angle being only a small fraction of $2\theta_B$ [see *IT* B (1996, Part 5)]. Radiation of a given wavelength coming from a small source at S and undergoing Bragg

diffraction in $CC'D'D$ will take the path shown by the heavy line in Fig. 2.7.2.4, simplifying the picture to the case of extreme confinement of energy flow to parallelism with the Bragg planes. At the X-ray exit surface DD', splitting into $\mathbf{K}_0$ and $\mathbf{K}_h$ beams occurs. A slit-less arrangement, as shown in the figure, may suffice. Then, when S is a point-like source of $K\alpha$ radiation, and distance a is sufficiently large, films F_1 and F_2 will each record a pair of narrow images formed by the α_1 and α_2 wavelengths, respectively. A wider area of specimen can be imaged if a line focus rather than a point focus is placed at S (Barth & Hosemann, 1958), but then the α_1 and α_2 images will overlap. Under conditions of high anomalous transmission, defects in the crystal cause a reduction in transmitted intensity, which appears similarly in the $\mathbf{K}_0$ and $\mathbf{K}_h$ images. Thus, it is possible to gain intensity and improve resolution by recording both images superimposed on a film F_3 placed in close proximity to the X-ray exit face DD' (Gerold & Meier, 1959).

2.7.3. Double-crystal topography

The foregoing description of single-crystal techniques will have indicated that in order to gain greater sensitivity in orientation contrast there are required incident beams with closer collimation, and limitation of dispersion due to wavelength spread of the characteristic X-ray lines used. It suggests turning to prior reflection of the incident beam by a perfect crystal as a means of meeting these needs. Moreover, the application of crystal-reflection-collimated radiation to probe angularly step by step as well as spatially point by point the intensity of Bragg reflection from the vicinity of an individual lattice defect such as a dislocation brings possibilities of new measurements beyond the scope provided by simply recording the local value of the integrated reflection. The X-ray optical principles of double-crystal X-ray topography are basically those of the double-crystal spectrometer (Compton & Allison, 1935). The properties of successive Bragg reflection by two or more crystals can be effectively displayed by a Du Mond diagram (Du Mond 1937), and such will now be applied to show how collimation and monochromatization result from successive reflection by two crystals, U and V, arranged as sketched in Fig. 2.7.3.1. They are in the dispersive, antiparallel, '$++$' setting, and are assumed to be identical perfect crystals set for the same symmetrical Bragg reflection. Only rays making the same glancing angle with both surfaces will be reflected by both U and V. For example, radiation of shorter wavelength reflected at a smaller glancing angle at U (the ray shown by the dashed line) will impinge at a larger glancing angle on V and not satisfy the Bragg condition. In this $++$ setting, with a given angle ω between the Bragg-reflecting planes of each crystal, $\theta_U + \theta_V = \omega$ and $\Delta\theta_U = -\Delta\theta_V$. The Du Mond diagram for the $++$ setting, Fig. 2.7.3.2, shows plots of Bragg's law for each crystal, the V curve being a reflection of the U curve in a vertical mirror line and differing by ω from the U curve in its coordinate of intersection with the axis of abscissa, in accord with the equations given above. The small angular range of reflection of a monochromatic ray by each perfect crystal is represented exaggeratedly by the band between the parallel curves. Where the band for crystal U superimposes on the band for V (the shaded area) defines semiquantitatively the divergence and wavelength spread in the rays successively reflected by U and V. (It is taken for granted that $\frac{1}{2}\omega$ lies between the maximum and minimum incident glancing angles on U, $\theta_{\max}$ and $\theta_{\min}$, afforded by the incident beam, assumed polychromatic.) The reflected beam from U alone contains wavelengths ranging from $\lambda_{\min}$ to $\lambda_{\max}$. Comparison of these θ and λ ranges with the extent of the shaded area illustrates the efficacy of the $++$ arrangement in providing a collimated and monochromatic beam, which can be employed to probe the reflecting properties of a third crystal (Nakayama, Hashizume, Miyoshi, Kikuta & Kohra, 1973). Techniques employing three or more successive Bragg reflections find considerable application when used with synchrotron X-ray sources, and will be considered below, in Section 2.7.4.

The most commonly used arrangement for double-crystal topography is shown in Fig. 2.7.3.3, in which U is the 'reference' crystal, assumed perfect, and V is the specimen crystal under examination. Crystals U and V are in the parallel, '$+-$' setting, which is non-dispersive when the Bragg planes of U and V have the same (or closely similar) spacings. Before considering the Du Mond diagram for this arrangement, note that Bragg reflection at the reference crystal U is asymmetric, from planes inclined at angle α to its surface. Asymmetric reflections have useful properties, discussed, for example, by Renninger (1961), Kohra (1972), Kuriyama & Boettinger (1976), and Boettinger, Burdette & Kuriyama (1979). The asymmetry factor, b, of magnitude $|\mathbf{K}_0 \cdot \mathbf{n}/\mathbf{K}_h \cdot \mathbf{n}|$, $\mathbf{n}$ being the

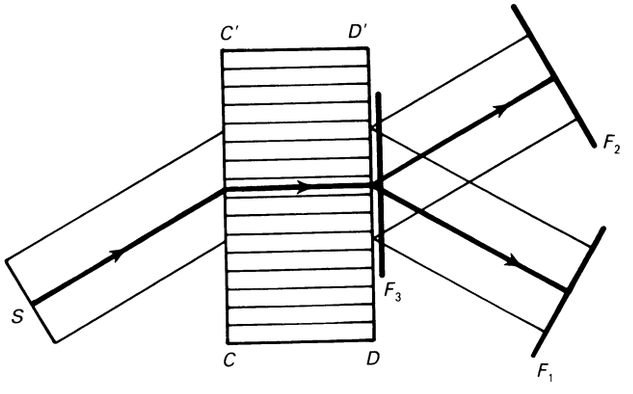

Fig. 2.7.2.4. Topographic techniques using anomalous transmission.

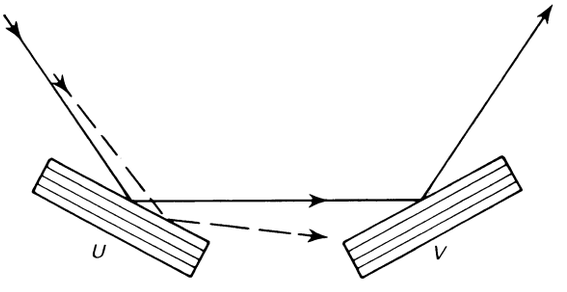

Fig. 2.7.3.1. Double-crystal $++$ setting.

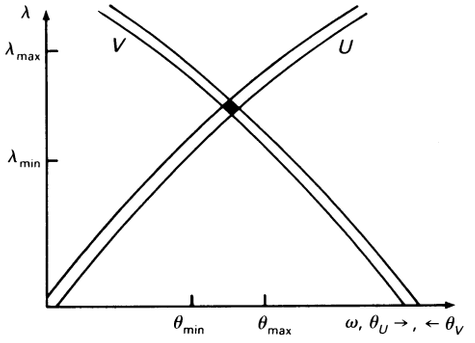

Fig. 2.7.3.2. Du Mond diagram for $++$ setting in Fig. 2.7.3.1.

crystal-surface normal, is also the ratio of spatial widths of the incoming to the outgoing beams, W_{in}/W_{out}. In the case of symmetric Bragg reflection, the perfect crystal U would totally reflect (in the zero-absorption case) over a small angular range, w_S. In the asymmetric case, the ranges of total reflection are w_{in} for the incoming rays and w_{out} for the outgoing. Dynamical-diffraction theory [*IT* B (1996, Part 5)] shows that $w_{out} = bw_{in} = b^{1/2} w_S$, so that $w_{in}W_{in} = w_{out}W_{out}$ (as would be expected from energy conservation). Thus, highly asymmetric reflection from the reference crystal U not only provides a spatially wide beam, able to cover a large area of V without recourse to any mechanical traversing motion of the components S, U or V, but also produces a desirably narrow angular probe for studying the angular breadth of reflection of V. In practice, values of b lower than 0.1 can be used.

Du Mond diagrams for the $+-$ arrangement are shown in Fig. 2.7.3.4(*a*) and (*b*). For simplicity, the curves (slope $d\lambda/d\theta = 2d\cos\theta$) are represented by straight lines. In the $+-$ setting, $\theta_V - \theta_U = \omega$ and $\Delta\theta_V = \Delta\theta_U$. In Fig. 2.7.3.4(*a*), the narrow band labelled U passing through the origin represents the beam of angular width w_{out} leaving U. It is assumed that all of the specimen crystal V has the same interplanar spacing as U but that it contains a slightly misoriented minor region V'(which may be located as shown in Fig. 2.7.3.3). When ω differs substantially from zero, the bands corresponding to crystal V and its minor part V' lie in positions V_1 and V_1', respectively, in Fig. 2.7.3.4(*a*). (Only the relevant part of the latter band is drawn, for simplicity.) The offset along the θ axis between V_1 and V_1' is the component $\Delta\varphi$ of the misorientation between V and V' that lies in the plane of incidence. If ω is reduced step-wise, a double-crystal topograph image being obtained at F at each angular setting, $\Delta\varphi$ can be found from film densitometry, which will show at what settings band U is most effectively overlapped by band V or by band V'. When ω is reduced to zero, the specimen crystal bands are at V_2 and V_2'. The drawing shows that V' has then passed right through the setting for its Bragg reflection, which occurred at a small positive value of ω. Since the U and V bands have identical slopes, their overlap occurs at all wavelengths when $\omega = 0$. In practice, only the shaded area is involved, corresponding to the wavelength range λ_{min} to λ_{max}, defined by the range of incidence angles, θ_{min} to θ_{max}, on the Bragg planes of crystal U. (The width of band U will generally be negligible compared with the range of θ allowed by source width and slit collimation system.) One component of $\Delta\varphi$ is found in the procedure just described. The second component needed to specify the difference between **h**-vector directions of the Bragg planes of V and V' is obtained by repeating the experiment after rotating V by 90° about **h**.

Next consider the more general case when V' differs from V in both orientation and interplanar spacing, and both V' and V have slightly different interplanar spacings from U. The difference in orientation between V' and V, $\Delta\varphi$, and their difference in interplanar spacing, $d(V') - d(V)$, can be distinguished by taking two series of double-crystal topographs, the orientation of the specimen in its own plane (its azimuthal angle, ψ) being changed by a 180° rotation about its **h** vector between taking the first and second series. As shown schematically in the Du Mond diagram, Fig. 2.7.3.4(*b*), the U, V, and V' bands now all have slightly different slopes. [Reference crystal U is reflecting the same small wavelength band as in Fig. 2.7.3.4(*a*).] The setting represented in the diagram is that putting V at the maximum of its Bragg reflection Let the V' band be then at position V_0', for the case when $\psi = 0°$. Assume that, when ψ is changed by 180°, the rotation of the specimen in its own plane can be made about the **h** vector of V precisely. (This assumption simplifies the diagram.) Then this 180° rotation will not cause any translation of the V band along the θ axis, but does transfer the V' band from V_0' to the position V_{180}'. With the sense of increasing ω taken as that translating the specimen bands to the right and $\Delta\omega$ taken as the difference in readings between peak reflection from V and that from V', the diagram shows that, with $\psi = 0°$, $\Delta\omega_0 = \theta(V') - \theta(V) + \Delta\varphi$, and, with $\psi = 180°$,

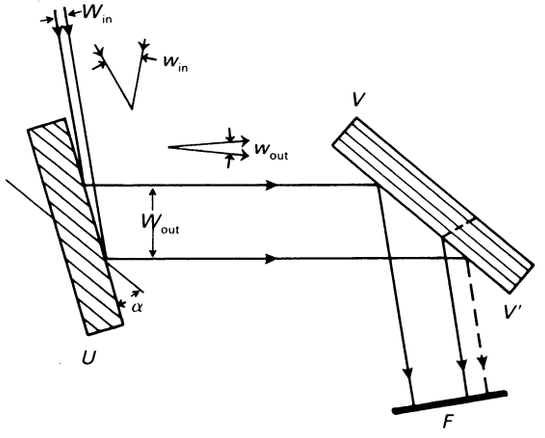

Fig. 2.7.3.3. Double-crystal topographic arrangement, $+-$ setting. Asymmetric reflection from reference crystal U. Specimen crystal divided into regions V and V'.

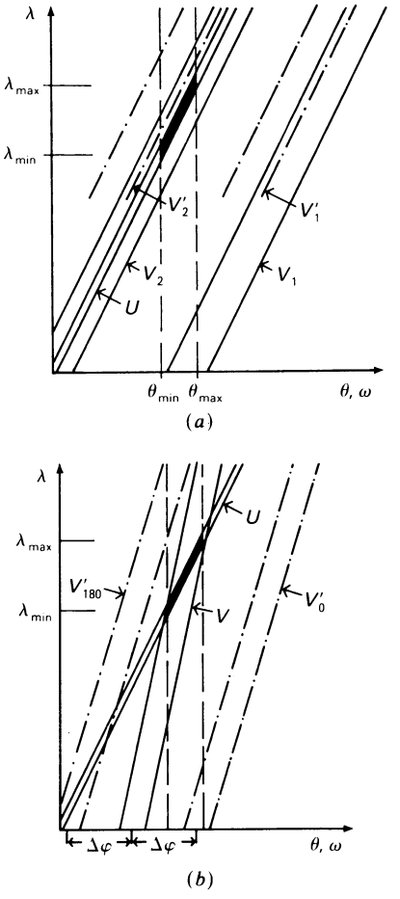

Fig. 2.7.3.4. Du Mond diagrams for $+-$ setting in Fig. 2.7.3.3. (*a*) Case when specimen region V' is misoriented with respect to V, but U, V, and V' all have the same interplanar spacing. (*b*) Case when V' differs from V in both orientation and interplanar spacing, and both differ from U in interplanar spacing.

$\Delta\omega_{180} = \theta(V') - \theta(V) - \Delta\varphi$, from which both $\Delta\varphi$ and the difference in Bragg angles can be found. The interplanar spacing difference is given by $d(V') - d(V) = [\theta(V) - \theta(V')]d \cot\theta$, d being the mean interplanar spacing of V and V'. In practice, series of topographs are taken with azimuthal angles $\psi = 0$, 90, 180, and 270°, so that the two components needed to specify the misorientation vector between the Bragg-plane normals of V and V' can be determined. The Du Mond diagram shows that in this slightly dispersive experiment the range of overlap of the U band with any V band can be restricted by reducing the angular range or wavelength range of rays incident on U. Such reduction can be achieved by use of a small source S far distant from U, such as a synchrotron source. It can also be achieved by methods described in Subsection 2.7.4.2. As regards spatial resolution on double-crystal topographs, relations analogous to those for single-crystal topographs apply. If the reference crystal U unavoidably contains some defects, their images on F can deliberately be made diffuse compared with images of defects in V by making the UV distance relatively large. In a nearly dispersion-free arrangement, if the $K\alpha_1$ wavelength is being reflected, then so too will the $K\alpha_2$ if S is sufficiently widely extended in the incidence plane, as is usually necessary to image a usefully large area of V. If the distance VF cannot be made sufficiently small to reduce to a tolerable value the resolution loss due to simultaneous registration of the α_1 and α_2 images, then a source S of small apparent size, together with a collimating slit before U, will be needed. In order to obtain imaging of a large area of V, a linear scanning motion to and fro at an angle to SU in the plane of incidence must be performed by the source and collimator relative to the double-crystal camera. Whether it is the source and collimator or the camera that physically move depends upon their relative portability. When the source is a standard sealed-off X-ray tube, it is not difficult to arrange for it to execute the motion (Milne, 1971).

In some applications, it may occur that the specimen is so deformed that only a narrow strip of its surface will reflect at each ω setting. Then, a sequence of images can be superimposed on a single film, changing ω by a small step between each exposure. The 'zebra' patterns so obtained define contours of equal 'effective misorientation', the latter term describing the combined effect of variations in tilt $\Delta\varphi$ and of Bragg-angle changes due to variations in interplanar spacing (Renninger, 1965; Jacobs & Hart, 1977).

Double-crystal topography employing the parallel setting was developed independently by Bond & Andrus (1952) and by Bonse & Kappler (1958), and used by the former workers for studying reflections from surfaces of natural quartz crystals, and by the latter for detecting the strain fields surrounding outcrops of single dislocations at the surfaces of germanium crystals. Since then, the method has been much refined and widely applied. The detection of relative changes in interplanar spacing with a sensitivity of 10^{-8} is achievable using high-angle reflections and very perfect crystals. These developments have been reviewed by Hart (1968, 1981).

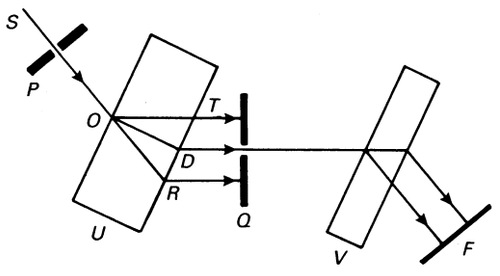

Fig. 2.7.3.5. Transmission double-crystal topography in + − setting with spatial limitation of beam leaving reference crystal.

Transmitted Bragg reflection (*i.e.* the Laue case) can be used for either or both crystals U and V, in both the + + and + − settings, if desired. When the reference crystal U is used in transmission, a technique due to Chikawa & Austerman (1968), shown in Fig. 2.7.3.5, can be employed if U is relatively thick and, preferably, not highly absorbing of the radiation used. This technique exploits a property of diffraction by ideally perfect crystals, that, for waves satisfying the Bragg condition exactly, the energy-flow vector (Poynting vector) within the energy-flow triangle (the triangle ORT in Figs. 2.7.2.2 and 2.7.2.3) is parallel to the Bragg planes. (In fact, the energy-flow vectors swing through the triangle ORT as the range of Bragg reflection is swept by the incident wave vector, $\mathbf{K}_0$.) Placing a slit Q as shown in Fig. 2.7.3.5 so as to transmit only those diffracted rays emerging from RT whose energy-flow direction in the crystal ran parallel, or nearly parallel, to the Bragg plane OD has the effect of selecting out from all diffracted rays only those that have zero or very small angular deviation from the exact Bragg condition. The slit Q thus provides an angularly narrower beam for studying the specimen crystal V than would be obtained if all diffracted rays from U were allowed to fall on V. The specimen is shown here in the + − setting, and also oriented to transmit its diffracted beam to the film F. This specimen arrangement is a likely embodiment of the technique but is incidental to the principle of employing *spatial* selection of transmitted diffraction rays to gain *angular* selection, a technique first used by Authier (1961). A practical limitation of this technique arises from angular spreading due to Fraunhofer diffraction by the slit Q: use of too fine an opening of Q will defeat the aim of securing an extremely angularly narrow beam for probing the specimen crystal.

2.7.4. Developments with synchrotron radiation

2.7.4.1. *White-radiation topography*

The generation and properties of synchrotron X-rays are discussed by Arndt in Subsection 4.2.1.5. For reference, his list of important attributes of synchrotron radiation is here repeated as follows: (1) high intensity, (2) continuous spectrum, (3) narrow angular collimation, (4) small source size, (5) polarization, (6) regularly pulsed time structure, and (7) computability of properties. All these items influence the design and scope of X-ray topographic experiments with synchrotron radiation, in some cases profoundly. The high intensity of continuous radiation delivered in comparison with the output of standard X-ray tubes, and hence the rapidity with which X-ray topographs could be produced, was the first attribute to attract attention, through the pioneer experiments of Tuomi, Naukkarinen & Rabe (1974), and of Hart (1975*a*). They used the simple diffraction geometry of the Ramachandran (Fig. 2.7.1.2) and Schulz (Fig.2.7.1.1) methods, respectively. [Since in the transmission-specimen case a multiplicity of Laue images can be recorded, it is usual to regard this work as a revival of the Guinier & Tennevin (1949) technique.] Subsequent developments in synchrotron X-ray topography have been reviewed by Tanner (1977) and by Kuriyama, Boettinger & Cohen (1982), and described in several chapters in Tanner & Bowen (1980). Some developments of methods and apparatus that have been stimulated by the advent of synchrotron-radiation sources will be described in this and in the following Subsection 2.7.4.2, the division illustrating two recognizable streams of development, the first exploiting the speed and relative instrumental simplicity

of white-radiation synchrotron X-ray topography, the second directed towards developing sophisticated 'beam conditioners' to extract highly collimated and monochromatic beams from the continuous-wavelength output of the synchrotron source. In both monochromatic and continuous-radiation experiments, the high intensity renders it more practicable than with conventional sources to apply electronic 'real-time' imaging systems (discussed in Sections 7.1.6 and 7.1.7, and Subsection 2.7.5.2).

At the experimental stations where synchrotron X-ray topography is performed, the distance a from the source (the tangent point on the electron orbit) is never less than some tens of metres, *e.g.* 40 m at the Deutsches Elektronen-Synchrotron, Hamburg (DESY), a maximum of 80 m at the Synchrotron Radiation Source, Daresbury (SRS), and 140 m at the European Synchrotron Radiation Facility (ESRF). The dimensions of the X-ray source (given by the cross section of the electron beam at the tangent point) vary widely between different installations (see Table 4.2.1.7), but the dimension in the plane of the electron orbit is usually several times that normal to it. If W_x and W_z are the corresponding full widths at half-maximum intensity of the source, then with the simple X-ray optics of a white-radiation topograph the geometrical resolution will be $W_x b/a$ and $W_z b/a$ in the orbit-plane (horizontal) and normal to the orbit-plane (vertical) directions, respectively, independent of the orientation of the plane of incidence of the Bragg reflection concerned. Representative dimensions might be $W_x = 2$ mm, $W_z = 0.5$ mm, and $a = 50$ m. With $b = 100$ mm, the horizontal and vertical resolutions of the topograph image would then be 4 and 1 μm, respectively, comparable with those on a conventional source, but with $b = 10$ mm only. Thus, even under synchrotron-source conditions, it is desirable that b should not exceed some centimetres in order to avoid geometrical factors causing a severer limitation of resolution (at least in one dimension) than other factors [such as photo-electron track lengths in the emulsion and point-by-point statistical fluctuations in absorbed photon dose (Lang, 1978)]. Since synchrotron X-rays are generated at all points along a curved electron trajectory, they spread out in a sheet parallel to the orbit plane. So there is in principle no limit to the specimen dimension in that plane that can be illuminated in a white-radiation topograph. However, increased background due to scattering from air and other sources imposes a practical limit of around 100 mm on the beam width. With electrons circulating in a planar orbit, the divergence of radiation normal to the orbit plane is strongly constricted, significant intensity being contained only within a fan of opening angle $\Omega \simeq mc^2/E$, *e.g.* $\Omega = 0.25$ mrad with electron energy $E = 2$ GeV, equivalent to a vertical distance $\sim$12 mm with $a = 50$ m. This does impose a significant restriction on the area of specimen that can be imaged in a transmission topograph unless recourse be had to beam expansion by an asymmetrically reflecting monochromator crystal.

For analysis of the three-dimensional configuration of defects within crystals, it is a useful feature of white-radiation transmission topography that different views of the specimen are presented simultaneously by the assemblage of Laue images, and that when studying reflection from a given Bragg plane there is freedom to vary the glancing angle upon it. When interpreting the diffraction contrast effects observed, the relative contributions of all the diffraction orders superimposed must be considered. However, after taking into account source spectral distribution, specimen structure factors, absorption losses and film efficiency, it is often found that a particular order of reflection is dominant in each Laue image (Tuomi, Naukkarinen & Rabe, 1974; Hart, 1975*a*). The variation of diffraction contrast with wavelength follows different trends for different types of defect (Lang, Makepeace, Moore & Machado, 1983), so the ability to vary the wavelength with which a given order of reflection is studied can help in identifying the type of defect.

If the orbiting electrons are confined to a plane, then the radiation emitted in that plane is completely linearly polarized with the **E** vector in that plane. It follows that diffraction with the plane of incidence normal to the orbit plane is in pure σ-polarization mode (polarization factor $P = 1$), and with plane of incidence parallel to the orbit plane in pure π-polarization mode ($P = |\cos 2\theta_B|$). The former, vertical plane of incidence is often chosen to avoid vanishing of reflections in the region of $2\theta_B = 90°$. The ability to record patterns with either pure σ-mode or pure π-mode polarization is very helpful in the study of several dynamical diffraction phenomena. To facilitate switching of polarization mode, some diffractometers and cameras built for use with synchrotron sources are rotatable bodily about the incident-beam axis (Bonse & Fischer, 1981; Bowen, Clark, Davies, Nicholson, Roberts, Sherwood & Tanner, 1982; Bowen & Davies, 1983). From the diffraction-theoretical standpoint, it is the section topograph that provides the image of fundamental importance. High-resolution section-topograph patterns have been recorded with synchrotron radiation using a portable assembly combining crystal mount and narrow incident-beam slit. With the help of optical methods of alignment, this can be transferred between topograph cameras set up at a conventional source and at the synchrotron source (Lang, 1983).

The regularly pulsed time structure of synchrotron radiation can be exploited in stroboscopic X-ray topography. The wavefronts of travelling surface acoustic waves (SAW) on lithium niobate crystals have been imaged, and their perturbation by lattice defects disclosed (Whatmore, Goddard, Tanner & Clark, 1982; Cerva & Graeff, 1984, 1985). The latter workers made detailed studies of the relative contributions to the image made by orientation contrast and by 'wavefield deviation contrast' (*i.e.* contrast arising from deviation of the energy-flow vector in the elastically strained crystal).

2.7.4.2. *Incident-beam monochromatization*

In order to achieve extremely small beam divergences and wavelength pass bands ($d\lambda/\lambda$), and, in particular, to suppress transmission of harmonic wavelengths, arrangements much more complicated than the double-crystal systems shown in Figs. 2.7.3.1 and 2.7.3.3 have been applied in synchrotron-radiation topography. The properties of monochromator crystals are discussed in Section 4.2.5. In synchrotron-radiation topographic applications, the majority of monochromators are constructed from perfect silicon, with occasional use of germanium. Damage-free surfaces of optical quality can be prepared in any orientation on silicon, and smooth-walled channels can be milled into silicon monoliths to produce multireflection devices. First, for simpler monochromatization systems, one possibility is to set up a monochromator crystal oriented for Bragg reflection with asymmetry $b \gg 1$ (*i.e.* giving $W_{\rm out}/W_{\rm in} \ll 1$) to produce a narrow monochromatic beam with which section topographs can be taken (Mai, Mardix & Lang, 1980). The standard $+-$ double-crystal topography arrangement is frequently used with synchrotron sources, the experimental procedure being as described in Section 2.7.3 and benefiting from the small divergence of the incident beam due to remoteness of the source. An example of a more refined angular probe is that obtainable by employing a pair of silicon crystals in $++$ setting to prepare the beam

Table 2.7.4.1. *Monolithic monochromator for plane-wave synchrotron-radiation topography*

Reflection 1	$\bar{3}33$
Reflection 2	$\bar{1}3\bar{1}$
Reflection 3	$1\bar{3}\bar{1}$
Output wavelength	0.12378 nm
Spectral pass band, $d\lambda/\lambda$	$\sim 7 \times 10^{-6}$
Angular divergence of exit beam	$\sim 1.4 \times 10^{-6}$
Size of exit beam	15×15 mm

incident on the specimen crystal, the three crystals together forming a $+ + -$ arrangement (Ishikawa, Kitano & Matsui, 1985). The first monochromator is oriented for asymmetric $11\bar{1}$ Bragg reflection, the second for highly asymmetric $55\bar{3}$ reflection ($W_{out}/W_{in} = 64$ at $\lambda = 0.12$ nm), resulting in a divergence of only 0.5×10^{-6} in the beam impinging on the specimen.

Multireflection systems, some of which were proposed by Du Mond (1937) but not at that time realizable, have become a practicality through the advent of perfect silicon and germanium. When multiple reflection occurs between the walls of a channel cut in a perfect crystal, the tails of the curve of angular dependence of reflection intensity can be greatly attenuated without much loss of reflectivity at the peak of the curve (Bonse & Hart, 1965*a*). Beaumont & Hart (1974) described combinations of such 'channel-cut' monochromators that were suitable for use with synchrotron sources. One combination, consisting of a pair of contra-rotating channel-cut crystals, with each channel acting as a pair of reflecting surfaces in symmetrical $+ -$ setting, has found much favour as a monochromatizing device producing neither angular deviation nor spatial displacement of the final beam, whatever the wavelength it is set to pass. The properties of monoliths with one or more channels and employing two or more asymmetric reflections in succession have been analysed by Kikuta & Kohra (1970), Kikuta (1971), and Matsushita, Kikuta & Kohra (1971).

Symmetric channel-cut monochromators in perfect undistorted crystals transmit harmonic reflections. Several approaches to the problem of harmonic elimination may be taken, such as one of the following procedures (or possibly more than one in combination).

(1) Using crystals of slightly different interplanar spacing (*e.g.* silicon and germanium) in the $+ -$ setting, which then becomes slightly dispersive (Bonse, Materlik & Schröder, 1976; Bauspiess, Bonse, Graeff & Rauch, 1977).

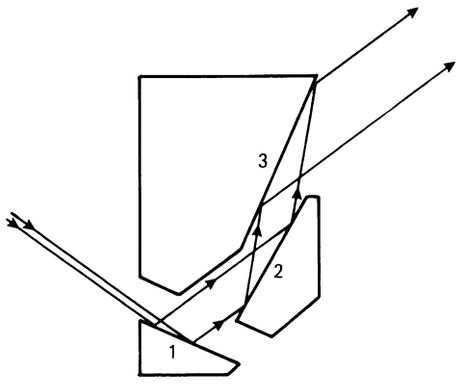

Fig. 2.7.4.1. Monolithic multiply reflecting monochromator for plane-wave topography.

(2) Laue case (transmission) followed by Bragg case (reflection), with deliberate slight misorientation between the diffracting elements (Materlik & Kostroun, 1980).

(3) Asymmetric reflection in non-parallel channel walls in a monolith (Hashizume, 1983).

(4) Misorientating a multiply reflecting channel, either one wall with respect to the opposite wall, or one length segment with respect to a following length segment (Hart & Rodrigues, 1978; Bonse, Olthoff-Münter & Rumpf, 1983; Hart, Rodrigues & Siddons, 1984).

For X-ray topographic applications, it is very desirable to have a spatially wide beam issuing from the multiply reflecting device. This is achieved, together with small angular divergence and spectral window, and without need of mechanical bending, in a monolith design by Hashizume, though it lacks wavelength tunability (Petroff, Sauvage, Riglet & Hashizume, 1980). The configuration of reflecting surfaces of this monolith is shown in Fig. 2.7.4.1. Reflection occurs in succession at surfaces 1, 2, and 3. The monochromator characteristics are listed in Table 2.7.4.1. The wavelength is very suitable in many topographic applications, and this design has proved to be an effective beam conditioner for use in synchrotron-radiation 'plane-wave' topography.

2.7.5. Some special techniques

2.7.5.1. *Moiré topography*

In X-ray optics, the same basic geometrical interpretation of moiré patterns applies as in light and electron optics. Suppose radiation passes successively through two periodic media, (1) and (2), whose reciprocal vectors are $\mathbf{h}_1$ and $\mathbf{h}_2$, so as to form a moiré pattern. Then, the reciprocal vector of the moiré fringes will be $\mathbf{H} = \mathbf{h}_1 - \mathbf{h}_2$. The magnitude, D, of the moiré fringe spacing is $|\mathbf{H}|^{-1}$ and may typically lie in the range 0.1 to 1 mm in the case of X-ray moiré patterns. Simple special cases are the 'rotation' moiré pattern in which $|\mathbf{h}_1| = |\mathbf{h}_2| = d^{-1}$, but $\mathbf{h}_1$ makes a small angle α with $\mathbf{h}_2$. Then, the spacing of the moiré fringes is d/α and the fringes run parallel to the bisector of the small angle α. The other special case is the 'compression' moiré pattern. Here, $\mathbf{h}_1$ and $\mathbf{h}_2$ are parallel but there is a small difference between their corresponding spacings, d_1 and d_2. The spacing D of compression moiré fringes is given by $D = d_1 d_2/(d_1 - d_2)$ and the fringes lie parallel to the grating rulings or Bragg planes in (1) and (2). X-ray moiré topographs achieve sensitivities of 10^{-7} to 10^{-8} in measuring orientation differences or relative differences in interplanar spacing. Moreover, if either periodic medium contains a lattice dislocation, Burgers vector $\mathbf{b}$, for which $\mathbf{b} \cdot \mathbf{h} \neq 0$, then a magnified image of the dislocation will appear in the moiré pattern, as one or more fringes terminating at the position of the dislocation, the number of terminating fringes being $\mathbf{b} \cdot \mathbf{h}$, which is necessarily integral (Hashimoto & Uyeda, 1957).

X-ray moiré topography has been performed with two quite different arrangements, the Bonse & Hart interferometer, and by superposition of separate crystals (Brádler & Lang, 1968). For accounts of the principles and applications of the interferometer, see, for example, Bonse & Hart (1965*b*, 1966), Hart (1968, 1975*b*), Bonse & Graeff (1977), Section 4.2.6 and §4.2.6.3.1. Fig. 2.7.5.1 shows the arrangement (Hart, 1968, 1972) for obtaining large-area moiré topographs by traversing the interferometer relative to a ribbon incident beam in similar fashion to taking a normal projection topograph (Fig. 2.7.2.2); P is the incident-beam slit, Q is a

stationary slit selecting the beam that it is desired to record, and film, *F*, and interferometer, *SMA*, together traverse to and fro as indicated by the double-headed arrow. In Fig. 2.7.5.1, *S*, *M*, and *A* are the three equally thick wafers of the interferometer that remain upstanding above the base of the monolithic interferometer after the gaps between *S* and *M*, and *M* and *A*, have been milled away. The elements *S*, *M* and *A* are called the splitter, mirror, and analyser, respectively. The moiré pattern is formed between the Bragg planes of *A* and the standing-wave pattern in the overlapping $\mathbf{K}_0$ and $\mathbf{K}_h$ beams entering it. Maximum fringe visibility occurs in the emerging beam that the slit *Q* is shown selecting. A dislocation will appear in the moiré pattern whether the lattice dislocation lies in *S*, *M*, or *A*, provided $\mathbf{b} \cdot \mathbf{h} \neq 0$. Moiré patterns formed in a number of Bragg reflections whose normals lie in, or not greatly inclined to, the plane of the wafers, can be recorded by appropriate orientation of the monolith. By this means, it is easily discovered in which wafer the dislocation lies, and its Burgers vector can be completely determined, including its sense, the latter being found by a deliberate slight elastic deformation of the interferometer (Hart, 1972). Satisfactory moiré topographs have been obtained with an interferometer in a synchrotron beam, despite thermal gradients due to the local intense irradiation (Hart, Sauvage & Siddons, 1980).

Fig. 2.7.5.2 shows crystal slices (1), *ABCD*, and (2), *EFGH*, superposed and simultaneously Bragg reflecting in the Brádler–Lang (1968) method of X-ray moiré topography. The slices could have been cut from separate crystals. In the case when the Bragg planes of (1) and (2) are in identical orientation but have a translational mismatch across *CD* and *EF* with a component parallel to **h**, strong scattering occurs towards *Z* as focus, producing extra intensity at T' in the $\mathbf{K}_0$ beam TT'' and at R' in the $\mathbf{K}_h$ beam RR''. It is usual to record the moiré pattern using the $\mathbf{K}_h$ beam. Projection moiré topographs are obtained by the standard procedure of traversing the crystal pair and film together with respect to the incident beam *SO*. The special procedure devised for mutually aligning the two crystals so that $\mathbf{h}_1$ and $\mathbf{h}_2$ coincide within their angular range of reflection is explained by Brádler & Lang (1968). This method has been applied to silicon and to natural (Lang, 1968) and synthetic quartz (Lang, 1978).

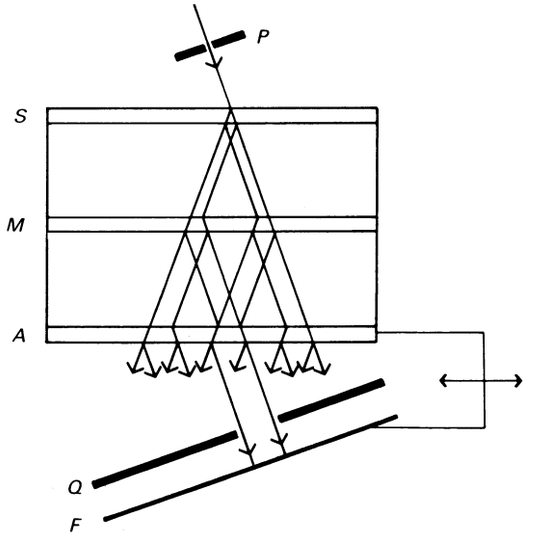

Fig. 2.7.5.1. Scanning arrangement for moiré topography with the Bonse–Hart interferometer.

2.7.5.2. *Real-time viewing of topograph images*

Position-sensitive detectors involving the production of electrons are described in Chapter 7.1, Sections 7.1.6 and 7.1.7, and Arndt (1986, 1990). Those descriptions cover all the image-forming devices that form the core of systems set up for 'live' X-ray topography. Here, discussion is limited to remarks on the historical development of techniques designed for making X-ray topographic images directly visible, and on the leading systems that are now sufficiently developed to be acceptable for routine use, in particular on topograph cameras set up at synchrotron X-ray sources. Two types of system became practicalities about the same time, that using direct conversion of X-rays to electronic signals by means of an X-ray-sensitive vidicon television camera tube (Chikawa & Fujimoto, 1968), and the indirect method using an external X-ray phosphor coupled to a multistage electronic image-intensifier tube (Reifsnider & Green, 1968; Lang & Reifsnider, 1969) or to a television-camera tube incorporating an image-intensifier stage (Meieran, Landre & O'Hara, 1969). These two approaches, the direct and the indirect, remain in competition. Developments up to the middle 1970's have been comprehensively reviewed by Hartman (1977). Since that time, Si-based, two-dimensional CCD (charge-coupled device) arrays have come into prominence as radiation detectors. They can be used for direct conversion of low-energy X-rays into electronic charges as well as for recording images of phosphor screens. As illustrated by Allinson (1994), four configurations employing CCD arrays for X-ray imaging can be considered: (i) direct detection by the 'naked' device; (ii) detection by phosphor coated directly on the CCD array; (iii) phosphor separate, and optically coupled to the CCD by lens or fibre-optics; and (iv) the addition to (iii) of an image intensifier

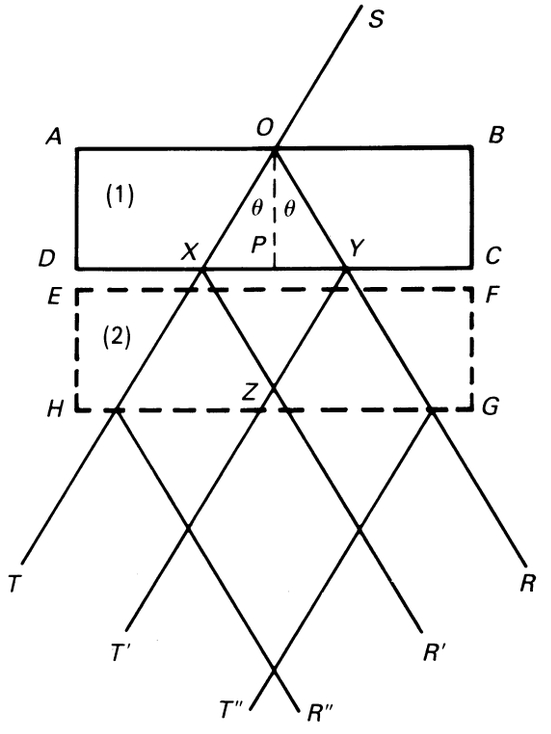

Fig. 2.7.5.2. Superposition of crystals (1) and (2) for production of moiré topographs. [Reproduced from *Diffraction and Imaging Techniques in Material Science*, Vol. II. *Imaging and Diffraction Techniques*, edited by S. Amelinckx, R. Gevers & J. Van Landuyt (1978), Fig. 21, p. 695. Amsterdam, New York, Oxford: North-Holland.]

or microchannel plate coupled to the phosphor screen. Consider first configuration (i). X-ray absorption efficiency in the active layer of silicon is near unity for radiations such as Cu $K\alpha$, and is not less than about 20% for Mo $K\alpha$ or Ag $K\alpha$. Since about one-third of the absorbed energy goes into electron–hole pair production, an absorbed 8 keV X-ray photon creates about 2000 pairs, a large number compared with a combined dark-current plus read-out noise level per photosite of a few tens of electrons r.m.s. Thus, single-photon counting is possible. Moreover, a cooled CCD can integrate the charge accumulated in each pixel for up to $\sim 10^3$ s. With pixel sizes in the range 10 to 30 μm square, and 1024×1024 (or 2048×2048) arrays in production, sensitive areas of 50 mm square, or greater, are available, sufficient for the majority of topographic applications.

For X-ray-sensitive TV-camera tubes, some major improvements in resolution and sensitivity have taken place since the first applications to X-ray topography of Be-windowed vidicons. Using the more sensitive 'Saticon' tube with incorporation of a 20 μm-thick Se–As target that provides good X-ray absorption efficiency, Chikawa, Sato & Fujimoto (1984) achieved a resolution as good as 6 μm at a modulation transfer function (MTF) of 5%. This betters that achieved with indirect systems or with standard-pixel-size CCD arrays used as direct detectors. The newer 'Harp' tube, which employs avalanche multiplication produced by a high field ($\sim 10^8$ V m^{-1}) applied across a 2 μm Se target to increase light sensitivity at least ten fold compared with the Saticon tube, has also been modified into a direct X-ray detector. Increasing the target thickness to 8 μm and adding an X-ray-transparent window provides satisfactory detector efficiency over a useful wavelength range (and the Se $K\alpha$-absorption edge at 0.098 nm causes absorption efficiencies for Cu $K\alpha$ and Mo $K\alpha$ to be similar, about 25%). The gain is sufficient for detection of single Cu $K\alpha$ photon-absorption events (at least for photons absorbed close to the target front, giving the maximum path for avalanche formation). A limiting resolution of about 25 μm (at MTF of ~33%) is exhibited (Sato, Maruyama, Goto, Fujimoto, Shidara, Kawamura, Hirai, Sakai & Chikawa, 1993), not yet as good as the 6 μm achieved with the Saticon tube. The rather small 6×9 mm sensitive areas of these camera tubes (when in standard '$\frac{2}{3}$ in' size) restricts their range of topographic applications as direct detectors compared with CCD arrays, but their amorphous Se targets are less likely to be degraded by X-radiation damage than crystalline-silicon CCD arrays. The latter do suffer degradation, but recover after treatment (Allinson, Allsopp, Quayle & Magorrian, 1991).

In the case of indirect systems, the lens or fibre-optic plate situated between phosphor and detector automatically protects the latter from radiation damage. Somewhat better resolution can be achieved by lens coupling than by fibre-optic coupling of phosphor to detector, but at the expense of loss of light-collection efficiency generally too great to be acceptable. In principle, magnification or de-magnification of the phosphor-screen image on the detector can be selected according to whether phosphor or detector has the better resolution, in order to maximize the system resolution as a whole. Phosphor resolution can be increased by diminishing its thickness below the value that would be chosen from consideration of X-ray absorption efficiency alone. Using a phosphor screen of Gd_2O_2S(Tb) only 5 μm thick, and lens-coupling it with tenfold magnification on to the target of a low-light-level television camera, Hartmann achieved a system resolution of about 10 μm (Queisser, Hartmann & Hagen, 1981), as good as any demonstrated so far with indirect systems.

The phosphors already used (or potentially usable) in real-time X-ray topography are inorganic compounds containing elements of medium or heavy atomic weight. They include ZnS(Ag), NaI(Tl), CsI(Tl), Y_2O_2S(Tb), Y_2O_2S(Eu), La_2O_2S(Eu) and Gd_2O_2S(Tb). Problems encountered are light loss by light trapping within single-crystal phosphor sheets, and resolution loss by light scattering from grain to grain in phosphor powders. Various ways of reducing lateral light-spreading within phosphor screens by imposing a columnar structure upon them have been tried. Most success has been achieved with CsI. Evaporated layers of this crystal have a natural tendency towards columnar cracking normal to the substrate. Then internal reflection within columns reduces 'cross talk' between columns (Stevels & Kühl, 1974). However, a columnar structure can be very effectively imposed on CsI films evaporated on to fibre-optic plates by etching away the cladding glass surrounding each fibre core to a depth of 10 μm, say. The evaporated CsI starts growing on the protruding cores, and continues as pillars physically separated and hence to a large degree optically separated from their neighbours (Ito, Yamaguchi & Oba, 1987; Allinson, 1994; Castelli, Allinson, Moon & Watson, 1994).

The drive to develop systems for 2D imaging of single-crystal or fibre diffraction patterns produced by synchrotron radiation that offer spatial resolution better than that within the grasp of position-sensitive multiwire gas proportional counters (say 100–200 μm) has produced several phosphor/fibre-optic/CCD combinations that with some modifications would be useful for real-time X-ray topography. Diffraction-pattern recording requires a sensitive area not less than about 50 mm in diameter, so most systems incorporate a fibre-optic taper to couple a larger phosphor screen with a small CCD array. Spatial resolution in the X-ray image cannot then be better than CCD pixel size multiplied by the taper ratio. In one system that has been fully described, this product is $20.5\ \mu m \times 2.6$, and a point-spread FWHM of 80 μm on a 51×51 mm input area was realised without benefit from a columnar-structure phosphor (Tate, Eikenberry, Barna, Wall, Lawrance & Gruner, 1995). More appropriate for X-ray topography would be unit-magnification optical coupling of phosphor with a CCD array of not less than 1024×1024 elements and not more than 20 μm square pixel size. With such a combination, a system resolution of ~25 μm should be achievable; and at a synchrotron X-ray topography station at least one device offering resolution no worse than this should be available. There is a scope for both high-resolution, small-sensitive-area and lower-resolution, large-sensitive-area imaging systems in real-time X-ray topography. It has been shown possible to incorporate both types in a single topography camera for use with synchrotron radiation (Suzuki, Ando, Hayakawa, Nittono, Hashizume, Kishino & Kohra, 1984).

2.6.2 (*cont.*)

Knop, W., Nierhaus, K. H., Nowotny, V., Niinikoski, T. O., Krumpolc, M., Rieubland, J. M., Rijlart, A., Schärpf, O., Schink, H.-J., Stuhrmann, H. B. & Wagner, R. (1986). *Polarised neutron scattering from dynamic polarised targets of biological origin*. *Helv. Phys. Acta*, **59**, 741–746.

Kostorz, G. (1979). *Small-angle scattering and its applications to materials science*. *Treatise on materials science and technology,* Vol. 15, edited by G. Kostorz, pp. 227–289. New York: Academic Press.

Kostorz, G. (1988). *Small-angle neutron scattering – metallurgical applications*. *Materials science forum,* Vols. 27/28, edited by M. M. Elcombe & T. J. Hicks, pp. 325–344. Aedermannsdorf, Switzerland: Trans Tech Publications.

Kratky, O. & Worthmann, W. (1947). *Über die Bestimmbarkeit der Konfiguration gelöster organischer Moleküle durch interferometrische Vermessung mit Röntgenstrahlen*. *Monatsh. Chem.* **76**, 263–281.

Lindner, P., May, R. P. & Timmins, P. A. (1992). *Upgrading the SANS instrument D11 at the ILL*. *Physica (Utrecht)*, B**180–181**, 967–972.

Lindner, P. & Oberthür, R. C. (1985). *Shear induced deformation of polystyrene coils in dilute solution from small angle neutron scattering. 1. Shear gradient apparatus and first results*. *Colloid Polym. Sci.* **263**, 443–453.

Lindner, P. & Oberthür, R. C. (1988). *Shear-induced deformation of polystyrene coils in dilute solution from small angle neutron scattering. 2. Variation of shear gradient, molecular mass and solvent viscosity*. *Colloid Polym. Sci.,* **263**, 443–453.

Luzzati, V., Tardieu, A., Mateu, L. & Stuhrmann, H. B. (1976). *Structure of human serum lipoprotein in solution. I. Theory and techniques of an X-ray scattering approach using solvents of variable density*. *J. Mol. Biol.* **101**, 115–127.

May, R. P., Ibel, K. & Haas, J. (1982). *The forward scattering of cold neutrons by mixtures of light and heavy water*. *J. Appl. Cryst.* **15**, 15–19.

May, R. P. & Nowotny, V. (1989). *Distance information derived from neutron low-Q scattering*. *J. Appl. Cryst.* **22**, 231–237.

Moore, P. B. (1980). *Small-angle scattering. Information content and error analysis*. *J. Appl. Cryst.* **13**, 168–175.

Nierhaus, K. H., Lietzke, R., May, R. P., Nowotny, V., Schulze, H., Simpson, K., Wurmbach, P. & Stuhrmann, H. B. (1983). *Shape determination of ribosomal proteins in situ*. *Proc. Natl Acad. Sci. USA*, **80**, 2889–2893.

Pavlov, M. Yu. & Serdyuk, I. N. (1987). *Three-isotropic substitutions method in small-angle neutron scattering*. *J. Appl. Cryst.* **20**, 105–110.

Pedersen, J. S., Posselt, D. & Mortensen, K. (1990). *Analytical treatment of the resolution function for small-angle scattering*. *J. Appl. Cryst.* **23**, 321–333.

Porod, G. (1951). *Die Röntgenkleinwinkelstreuung von dichtgepackten kolloiden Systemen*. *Kolloid Z.* **124**, 83–114.

Porod, G. (1982). *General theory*. *Small-angle X-ray scattering,* edited by O. Glatter & O. Kratky, pp. 17–51. London: Academic Press.

Salva-Ghilarducci, A., Simon, J. P., Guyot, P. & Ansara, I. (1983). *Precipitation in ternary Al–Zn–Ag alloys studied by isotropic contrast in neutron small angle scattering*. *Acta Metall.* **31**, 1705–1713.

Schelten, J. & Hossfeld, F. (1971). *Application of spline functions to the correction of resolution errors in small-angle scattering*. *J. Appl. Cryst.* **4**, 210–223.

Stuhrmann, H. B. (1970). *Interpretation of small-angle scattering functions of dilute solutions and gases. A representation of the structures related to a one-particle-scattering function*. *Acta Cryst.* A**26**, 297–306.

Stuhrmann, H. B., Haas, J., Ibel, K., de Wolf, B., Koch, M. H. J., Parfait, R. & Crichton, R. R. (1976). *New low resolution model for 50S subunit of Escherichia coli ribosomes*. *Proc. Natl Acad. Sci. USA*, **73**, 2379–2383.

Stuhrmann, H. B. & Kirste, R. G. (1965). *Elimination der intrapartikulären Untergrundstreuung bei der Röntgenkleinwinkelstreuung an kompakten Teilchen (Proteinen)*. *Z. Phys. Chem. Neue Folge,* **46**, 247–250.

Stuhrmann, H. B., Schärpf, O., Krumpolc, M., Niinikoski, T. O., Rieubland, M. & Rijllart, A. (1986). *Dynamic nuclear polarisation of nuclear matter*. *Eur. Biophys. J.* **14**, 1–6.

Timmins, P. A. & Zaccai, G. (1988). *Low resolution structures of biological complexes studied by neutron scattering*. *Eur. Biophys. J.* **15**, 257–268.

Wignall, G. D. (1987). *Neutron scattering*. *Encyclopedia of polymer science and engineering,* Vol. 10, 2nd ed., edited by J. I. Kroschwitz, pp. 112–184. New York: John Wiley.

Wignall, G. D. & Bates, F. S. (1987). *Absolute calibration of small-angle neutron scattering data*. *J. Appl. Cryst.* **20**, 28–40.

Wignall, G. D., Christen, D. K. & Ramakrishnan, V. (1988). *Instrumental resolution effects in small-angle neutron scattering*. *J. Appl. Cryst.* **21**, 438–451.

Witz, J. (1983). *Contrast variation of the small-angle neutron scattering of globular particles: the influence of hydrogen exchange*. *Acta Cryst.* A**39**, 706–711.

Zaccai, G. & Jacrot, B. (1983). *Small angle neutron scattering*. *Annu. Rev. Biophys. Bioeng.* **12**, 139–157.

Zaccai, G., Wachtel, E. & Eisenberg, H. (1986). *Solution structure of halophilic malate dehydrogenase from small-angle neutron and X-ray scattering and ultracentrifugation*. *J. Mol. Biol.* **190**, 97–106.

2.7

Allinson, N. M. (1994). *Development of non-intensified charge-coupled device area X-ray detectors*. *J. Synchrotron Rad.* **1**, 54–62.

Allinson, N. M., Allsopp, D. W. E., Quayle, J. A. & Magorrian, B. G. (1991). *Effects of soft X-ray irradiation on solid-state imagers*. *Nucl. Instrum. Methods*, A**310**, 267–272.

Armstrong, R. W. & Wu, C. C. (1973) *X-ray diffraction microscopy*. *Tools and techniques for microstructural analysis*, edited by J. L. McCall & W. M. Mueller, pp. 169–219. New York: Plenum.

Arndt, U. W. (1986). *X-ray position-sensitive detectors*. *J. Appl. Cryst.* **19**, 145–163.

Arndt, U. W. (1990). *X-ray television area detectors*. *Synchrotron Radiat. News*, **3**, 17–22.

Authier, A. (1961). *Etude de la transmission anormale des rayons X dans des cristaux de silicium. I. Case des cristaux parfaits*. *Bull. Soc. Fr. Minéral. Cristallogr.* **84**, 51–89.

2.7 (*cont.*)

Authier, A. (1970). *Ewald waves in theory and experiment (dynamical theory of X-ray diffraction). Advances in structure research by diffraction methods*, Vol. 3, edited by R. Brill & R. Mason, pp. 1–51. Oxford: Pergamon Press.

Authier, A. (1977). *Section topography. X-ray optics. Applications to solids*, edited by H.-J. Queisser, Chap. 5, pp. 145–189. Berlin: Springer.

Barrett, C. S. (1945). *A new microscopy and its potentialities. Trans. Am. Inst. Min. Metall. Pet. Eng.* **161**, 15–64.

Barth, H. & Hosemann, R. (1958). *Anwendung der Parallelstrahlmethode in Durchstrahlungsfall zur Prüfung des Kristallinneren mit Röntgen-Strahlen. Z. Naturforsch. Teil A*, **13**, 792–794.

Batterman, B. W. & Cole, H. (1964). *Dynamical diffraction of X-rays by perfect crystals. Rev. Mod. Phys.* **36**, 681–717.

Bauspiess, W., Bonse, U., Graeff, W. & Rauch, H. (1977). *A bicrystal monochromator of moderate wavelength resolution for use with X-rays or thermal neutrons. J. Appl. Cryst.* **10**, 338–343.

Beaumont, J. H. & Hart, M. (1974). *Multiple Bragg reflection monochromators for synchrotron X radiation. J. Phys. E,* **7**, 823–829.

Berg, W. F. (1931). *Über ein röntgenographische Methode zur Untersuchung von Gitterstörungen an Kristallen. Naturwissenschaften*, **19**, 391–396.

Boettinger, W. J., Burdette, H. E. & Kuriyama, M. (1979). *X-ray magnifier. Rev. Sci. Instrum.* **50**, 26–30.

Bond, W. L. & Andrus, J. (1952). *Structural imperfections in quartz crystals. Am. Mineral.* **37**, 622–632.

Bonse, U. & Fischer, K. (1981). *The new multi-purpose two-axis diffractometer for synchrotron X-rays at DORIS. Nucl. Instrum. Methods*, **190**, 593–603.

Bonse, U. & Graeff, W. (1977). *X-ray and neutron interferometry. X-ray optics. Applications to solids*, edited by H.-J. Queisser, Chap. 4, pp. 93–143. Berlin: Springer.

Bonse, U. & Hart, M. (1965*a*). *Tailless X-ray single-crystal reflection curves obtained by multiple reflection. Appl. Phys. Lett.* **7**, 238–240.

Bonse, U. & Hart, M. (1965*b*). *An X-ray interferometer. Appl. Phys. Lett.* **6**, 155–158.

Bonse, U. & Hart, M. (1966). *Moiré patterns of atomic planes obtained by X-ray interferometry. Z. Phys.* **190**, 455–467.

Bonse, U. & Kappler, E. (1958). *Röntgenographische Abbildung des Verzerrungsfeldes einzelner Versetszungen in Germanium-Einkristallen. Z. Naturforsch. Teil A*, **13**, 348–349.

Bonse, U., Materlik, G. & Schröder, W. (1976). *Perfect-crystal monochromators for synchrotron X-radiation. J. Appl. Cryst.* **9**, 233–230.

Bonse, U., Olthoff-Münter, K. & Rumpf, A. (1983). *Monolithic double-grooved-crystal monochromators with tunable harmonic supression for neutrons and X-rays. J. Appl. Cryst.* **16**, 524–531.

Bowen, D. K., Clark, G. F., Davies, S. T., Nicholson, J. R. S., Roberts, K. J., Sherwood, J. N. & Tanner, B. K. (1982). *The X-ray topography station at Daresbury Laboratory. Nucl. Instrum. Methods*, **195**, 277–284.

Bowen, D. K. & Davies, S. T. (1983). *The double-crystal X-ray camera at Daresbury Laboratory. Nucl. Instrum. Methods*, **208**, 725–729.

Brádler, J. & Lang, A. R. (1968). *Use of the Ewald sphere in aligning crystal pairs to produce X-ray moiré fringes. Acta Cryst.* A**24**, 246–247.

Castelli, C. M., Allinson, N. M., Moon, K. J. & Watson, D. L. (1994). *High spatial resolution scintillation screens coupled to CCD detectors for X-ray imaging applications. Nucl. Instrum. Methods*, A**348**, 649–653.

Cerva, H. & Graeff, W. (1984). *Contrast investigation of surface acoustic waves by stroboscopic topography. I. Orientation contrast. Phys. Status Solidi A*, **82**, 34–45.

Cerva, H. & Graeff, W. (1985). *Contrast investigation of surface acoustic waves by stroboscopic topography. II. Wavefield deviation contrast. Phys. Status Solidi A*, **87**, 507–516.

Chikawa, J.-I. & Austerman, S. B. (1968). *X-ray double-crystal method of analyzing microstrains with BeO single crystals. Advances in X-ray analysis*, Vol. 11, edited by J. B. Newkirk & G. R. Mallett, pp. 393–400. New York: Plenum.

Chikawa, J.-I. & Fujimoto, I. (1968). *X-ray diffraction topography with a vidicon television image system. Appl. Phys. Lett.* **13**, 387–389.

Chikawa, J.-I., Sato, F. & Fujimoto, I. (1984). *High-resolution topography detector. Acta Cryst.* A**40**, C403.

Compton, A. H. & Allison, S. K. (1935). *X-rays in theory and experiment*. New York: Van Nostrand.

Du Mond, J. W. M. (1937). *Theory of the use of more than two successive X-ray crystal reflections to obtain increased resolving power. Phys. Rev.* **52**, 872–883.

Gerold, V. & Meier, F. (1959). *Der röntgenographische Nachweiss von Versetzungen in Germanium. Z. Phys.* **155**, 387–394.

Guinier, A. & Tennevin, J. (1949). *Sur deux variantes de la méthode de Laue et leurs applications. Acta Cryst.* **2**, 133–138.

Hart, M. (1968). *'Perfect crystals'. A study of their structural defects. Sci. Prog. Oxford*, **56**, 429–447.

Hart, M. (1971). *Bragg reflection X-ray optics. Rep. Prog. Phys.* **34**, 435–490.

Hart, M. (1972). *A complete determination of dislocation Burgers vectors by X-ray interferometry. Philos. Mag.* **26**, 821–831.

Hart, M. (1975*a*). *Synchrotron radiation – its application to high-speed, high-resolution X-ray diffraction topography. J. Appl. Cryst.* **8**, 436–444.

Hart, M. (1975*b*). *Ten years of X-ray interferometry. Proc. R. Soc. London Ser. A*, **346**, 1–22.

Hart, M. (1981). *Bragg angle measurement and mapping. J Cryst. Growth*, **55**, 409–427.

Hart, M. & Rodrigues, A. R. D. (1978). *Harmonic-free single-crystal monochromators for neutrons and X-rays. J. Appl. Cryst.* **11**, 248–253.

Hart, M., Rodrigues, A. R. D. & Siddons, D. P. (1984). *Adjustable resolution Bragg reflection systems. Acta Cryst.* A**40**, 502–507.

Hart, M., Sauvage, M. & Siddons, D. P. (1980). *'White beam' synchrotron X-ray interferometry. Acta Cryst.* A**36**, 947–951.

Hartmann, W. (1977). *Live topography. X-ray optics. Applications to solids*, edited by H.-J. Queisser, Chap. 6, pp. 191–219. Berlin: Springer.

Haruta, K. (1965). *A new method of obtaining stereoscopic pairs of X-ray diffraction topographs. J. Appl. Phys.* **36**, 1789–1790.

Hashimoto, H. & Uyeda, R. (1957). *Detection of dislocation by the moiré pattern in electron micrographs. Acta Cryst.* **10**, 143.

Hashizume, H. (1983). *Asymmetrically grooved monolithic crystal monochromators for suppression of harmonics in synchrotron X-radiation. J. Appl. Cryst.* **16**, 420–427; erratum: **16**, 648.

2.7 (*cont.*)

Hildebrandt, G. (1982). *X-ray wave fields in perfect and nearly perfect crystals – theoretical background and recent applications*. *J. Phys. E*, **15**, 1140–1155.

International Tables for Crystallography (1996). Vol. B. Dordrecht: Kluwer Academic Publishers.

Ishikawa, T., Kitano, T. & Matsui, J. (1985). *Synchrotron plane wave X-ray topography of GaAs with a separate (+, +) monochro-collimator*. *Jpn. J. Appl. Phys. Part 2*, **24**, L968–L971.

Ito, M., Yamaguchi, M. & Oba, K. (1987). *CsI(Na) scintillation plate with high spatial resolution*. *IEEE Trans. Nucl. Sci.* **34**, 401–405.

Jacobs, L. & Hart, M. (1977). *An X-ray topographic study of large crystals for a bent-crystal gamma diffractometer*. *Nucl. Instrum. Methods*, **143**, 319–325.

Jiang, S.-S. & Lang, A. R. (1983). *Stacking fault contrast in X-ray diffraction: a high resolution experimental study*. *Proc. R. Soc. London Ser. A*, **388**, 249–271.

Kato, N. (1974). *X-ray diffraction*, by L. V. Azaroff, R. Kaplow, N. Kato, R. J. Weiss, A. J. C. Wilson & R. A. Young, Chaps. 3–5, pp. 176–438. New York: McGraw–Hill.

Kikuta, S. (1971). *X-ray crystal collimators using successive asymmetric diffractions and their applications to measurements of diffraction curves. II. Type I collimator*. *J. Phys. Soc. Jpn*, **30**, 222–227.

Kikuta, S. & Kohra, K. (1970). *X-ray crystal collimators using successive asymmetric diffractions and their applications to measurements of diffraction curves. I. General considerations on collimators*. *J. Phys. Soc. Jpn*, **29**, 1322–1328.

Kohra, K. (1972). *Dynamical asymmetric diffraction and its applications to X-ray optical systems*. *Proceedings of the VIth International Conference on X-ray Optics and Microanalysis*, edited by G. Shinoda, K. Kohra & T. Ichinokawa, pp. 35–45. Tokyo: University of Tokyo Press.

Kuriyama, M. & Boettinger, W. J. (1976). *On the angular divergence of out-going beams in an asymmetric diffraction geometry*. *Acta Cryst.* A**32**, 511–512.

Kuriyama, M., Boettinger, W. J. & Cohen, G. G. (1982). *Synchrotron radiation topography*. *Annu. Rev. Mater. Sci.* **12**, 23–50.

Lang, A. R. (1957). *A method for the examination of crystal sections using penetrating charactistic radiation*. *Acta Metall.* **5**, 358–364.

Lang, A. R. (1959*a*). *The projection topograph: a new method in X-ray diffraction microradiography*. *Acta Cryst.* **12**, 249–250.

Lang, A. R. (1959*b*). *Studies of individual dislocations in crystals by X-ray diffraction microradiography*. *J. Appl. Phys.* **30**, 1748–1755.

Lang, A. R. (1963). *Applications of 'limited projection topographs' and 'direct beam topographs' in X-ray diffraction topography*. *Br. J. Appl. Phys.* **14**, 904–907.

Lang, A. R. (1968). *X-ray moiré topography of lattice defects in quartz*. *Nature (London)*, **220**, 652–657.

Lang, A. R. (1974). *On the growth-sectorial dependence of defects in natural diamonds*. *Proc. R. Soc. London Ser. A*, **340**, 233–248.

Lang, A. R. (1978). *Techniques and interpretation in X-ray topography*. *Diffraction and imaging techniques in material science*, 2nd, revised edition, edited by S. Amelinckx, R. Gevers & J. Van Landuyt, pp. 623–714. Amsterdam: North-Holland.

Lang, A. R. (1983). *Compact device for X-ray section topography with synchrotron sources*. *Rev. Sci. Instrum.* **54**, 897–899.

Lang, A. R., Makepeace, A. P. W., Moore, M. & Machado, W. G. (1983). *On the variation of X-ray diffraction contrast with wavelength: a study with synchrotron radiation*. *J. Appl. Cryst.* **16**, 113–125.

Lang, A. R. & Reifsnider, K. (1969). *Rapid X-ray diffraction topography using a high-gain image intensifier*. *Appl. Phys Lett.* **15**, 258–260.

Mai, Z.-H., Mardix, S. & Lang, A. R. (1980). *A high-resolution section topograph technique applicable to synchrotron radiation sources*. *J. Appl. Cryst.* **13**, 180–187.

Materlik, G. & Kostroun, V. O. (1980). *Monolithic crystal monochromators for synchrotron radiation with order sorting and polarising properties*. *Rev. Sci. Instrum.* **51**, 86–94.

Matsushita, T., Kikuta, S. & Kohra, K. (1971). *X-ray crystal collimators using successive asymmetric diffractions and their applications to measurements of diffraction curves. III. Type II collimator*. *J. Phys. Soc. Jpn*, **30**, 1136–1144.

Meieran, E. S., Landre, J. K. & O'Hara, S. (1969). *Direct video imaging of X-ray topographs*. *Appl. Phys. Lett.* **14**, 368–371.

Milne, A. D. (1971). *Scanning source X-ray topography*. *J. Appl. Cryst.* **4**, 251–252.

Nakayama, K., Hashizume, H., Miyoshi, A., Kikuta, S. & Kohra, K. (1973). *Use of asymmetrical dynamical diffraction of X-rays for multiple-crystal arrangements of the* $(n_1, +n_2)$ *setting*. *Z. Naturforsch. Teil. A*, **28**, 632–638.

Newkirk, J. B. (1958). *Method for the detection of dislocations in silicon by X-ray extinction contrast*. *Phys. Rev.* **110**, 1465–1466.

Newkirk, J. B. (1959). *The observation of dislocations and other imperfections by X-ray extinction contrast*. *Trans. TMS–AIME*, **215**, 483–497.

Petroff, J. F., Sauvage, M., Riglet, P. & Hashizume, H. (1980). *Synchrotron-radiation plane-wave topography. I. Application to misfit dislocation imaging in III–V heterojunctions*. *Philos. Mag.* A**42**, 319–338.

Pinsker, Z. G. (1978). *Dynamical scattering of X-rays in crystals*. Berlin: Springer.

Queisser, H.-J., Hartmann, W. & Hagen, W. (1981). *Real-time X-ray topography: defect dynamics and crystal growth*. *J. Cryst. Growth*. **52**, 897–906.

Ramachandran, G. N. (1944). *X-ray topographs of diamond*. *Proc. Indian Acad. Sci. Sect. A*, **19**, 280–292.

Reifsnider, K. & Green, R. E. Jr (1968). *Image intensifier system for dynamic X-ray diffraction studies*. *Rev. Sci. Instrum.* **39**, 1651–1655.

Renninger, M. (1961). *Asymmetrische Bragg-Reflexion am Idealkrystall zur Erhöhung des Doppelspekrometer-Auflösungsvermögens*. *Z. Naturforsch. Teil. A*, **16**, 1110–1111.

Renninger, M. (1965). *Beitrage zur doppeldiffraktometrischen Kristall-Topographic mit Röntgenstrahlen I. Methodik und Ergebnisse typischer Art*. *Z. Angew. Phys.* **19**, 20–33.

Sato, F., Maruyama, H., Goto, K., Fujimoto, I., Shidara, K., Kawamura, T., Hirai, T., Sakai, H. & Chikawa, J.-I. (1993). *Characteristics of a new high-sensitivity X-ray imaging tube for video topography*. *Jpn. J. Appl. Phys.* **32**, 2142–2146.

Schulz, L. G. (1954). *Method of using a fine-focus X-ray tube for examining the surface of single crystals*. *J. Met: Trans. AIME*, **200**, 1082–1083.

Stevels, A. L. N. & Kühl, W. (1974). *New phosphors for X-ray image intensifier tubes*. *Medicamundi*, **19**, 3–7.

2.7 (*cont.*)

Suzuki, S., Ando, M., Hayakawa, K., Nittono, O., Hashizume, H., Kishino, S. & Kohra, K. (1984). *A high-speed X-ray topography camera for use with synchrotron radiation at the photon factory*. *Nucl. Instrum. Methods*, **227**, 584–592.

Tanner, B. K. (1976). *X-ray diffraction topography*. Oxford: Pergamon Presss.

Tanner, B. K. (1977). *Crystal assessment by X-ray topography using synchrotron radiation*. *Prog. Cryst. Growth Charact.* **1**, 23–56.

Tanner, B. K. & Bowen, D. K. (1980). Editors. *Characterization of crystal growth defects by X-ray methods*. New York: Plenum.

Tate, M. W., Eikenberry, E. F., Barna, S. L., Wall, M. E., Lawrance, J. L. & Gruner, S. M. (1995). *A large-format high-resolution area X-ray detector based on a fiber-optically bonded charge-coupled device (CCD)*. *J. Appl. Cryst.* **28**, 196–205.

Tuomi, T., Naukkarinen, K. & Rabe, P. (1974). *Use of synchrotron radiation in X-ray diffraction topography*. *Phys. Status Solidi A*, **25**, 93–106.

Van Mellaert, L. & Schwuttke, G. H. (1972). *Feedback control system for scanning X-ray topography*. *J. Appl. Phys.* **43**, 687–692.

Wallace, C. A. & Ward, R. C. C. (1975). *A high-resolution X-ray topographical technique for thin flexible crystal plates*. *J. Appl. Cryst.* **8**, 281–286.

Whatmore, R. W., Goddard, P. A., Tanner, B. K. & Clark, G. F. (1982). *Direct imaging of travelling Rayleigh waves by stroboscopic X-ray topography*. *Nature (London)*, **299**, 44–46.

2.8

Ando, M. & Hosoya, S. (1972). *Q-switch and polarization domains in antiferromagnetic chromium observed with neutron diffraction topography*. *Phys. Rev. Lett.* **29**, 281–285.

Ando, M. & Hosoya, S. (1978). *Size and behavior of antiferromagnetic domains in Cr directly observed with X-ray and neutron topography*. *J. Appl. Phys.* **49**, 6045–6051.

Baruchel, J. (1989). *The contribution of neutron and synchrotron radiation topography to the investigation of first-order magnetic phase transitions*. *Phase Transit.* **14**, 21–29.

Baruchel, J., Schlenker, M. & Palmer, S. B. (1990). *Neutron diffraction topographic investigations of 'exotic' magnetic domains*. *Nondestr. Test. Eval.* **5**, 349–367

Baruchel, J., Schlenker, M., Zarka, A. & Petroff, J. F. (1978). *Neutron diffraction topographic investigation of growth defects in natural lead carbonate single crystals*. *J. Cryst. Growth*, **44**, 356–362.

Boeuf, A., Lagomarsino, S., Rustichelli, F., Baruchel, J. & Schlenker, M. (1975). *White beam neutron topography*. *Phys. Status Solidi A*, **31**, K91–K93.

Davidson, J. B. & Case, A. L. (1976). *Applications of the fly's eye neutron camera: diffraction tomography and phase transition studies*. Proc. Conf. on Neutron Scattering, ORNL, USERDA CONF 760601–P2, pp. 1124–1135.

Davidson, J. B., Werner, S. & Arrott, A. S. (1974). *Neutron microscopy of spin density wave domains in chromium*. *AIP Conf. Proc.*, edited by C. D. Graham & J. J. Rhyne, Vol. 18, pp. 396–400.

Doi, K., Minakawa, N., Motohashi, H. & Masaki, N. (1971). *A trial of neutron diffraction topography*. *J. Appl. Cryst.* **4**, 528–530.

Dudley, M., Baruchel, J. & Sherwood, J. N. (1990). *Neutron topography as a tool for studying reactive organic crystals: a feasibility study*. *J. Appl. Cryst.* **23**, 186–198.

Hustache, R. (1979). *Sélection de blocs monocristallins dans un cristal de beryllium par topographie neutronique*. *Nucl. Instrum. Methods*, **163**, 151–156.

Malgrange, C., Petroff, J. F., Sauvage, M., Zarka, A. & Englander, M. (1976). *Individual dislocation images and Pendellösung fringes in neutron topographs*. *Philos. Mag.* **33**, 743–751.

Scherm, R. & Fåk, B. (1993). *Neutrons*. In *Neutron and synchrotron radiation for condensed matter studies*, Vol. 1: *Theory, instruments and methods*. *HERCULES (Higher European Research Course for Users of Large Experimental Systems)*, *Grenoble*, edited by J. Baruchel, J. L. Hodeau, M. S. Lehmann, J. R. Regnard & C. Schlenker. Les Ulis: Les Editions de Physique; Berlin: Springer-Verlag.

Schlenker, M., Baruchel, J., Perrier de la Bathie, R. & Wilson, S. A. (1975). *Neutron diffraction section topography: observing crystal slices before cutting them*. *J. Appl. Phys.* **46**, 2845–2848.

Schlenker, M. & Shull, C. G. (1973). *Polarized neutron techniques for the observation of ferromagnetic domains*. *J. Appl. Phys.* **44**, 4181–4184.

Sillou, D., Baruchel, J., Kuroda, K., Michalowicz, A., Guigay, J. P. & Schlenker, M. (1989). *First experiments on flipping ratio mapping with the 'multi-PM' position-sensitive detector*. *Physica (Utrecht)*, B**156–157**, 581–583.

Tomimitsu, H., Doi, K. & Kamada, K. (1983). *Neutron diffraction topographic observations of substructures in Cu-based alloys*. *Physica (Utrecht)*, B**120**, 96–102.

2.9

Berk, N. F. & Majkrzak, C. F. (1995). *Using parametric B-splines to fit specular reflectivities*. *Phys. Rev. B*, **51**, 11296–11309.

Boer, D. K. G. de (1994). *Influence of the roughness profile on the specular reflectivity of X-rays and neutrons*. *Phys. Rev. B*, **49**, 5817–5820.

Buttiker, M. (1983). *Larmor precession and the traversal time for tunneling*. *Phys. Rev. B*, **27**, 6178–6188.

Felcher, G. P., Hilleke, R. O., Crawford, R. K., Haumann, J., Kleb, R. & Ostrowski, G. (1987). *Polarized neutron reflectometer: a new instrument to measure magnetic depth profiles*. *Rev. Sci. Instrum.* **58**, 609–619.

Felcher, G. P. & Russell, T. P. (1991). Editors. *Physica (Utrecht)*, B**173**, 1–210.

Hamilton, W. A., Hayter, J. B. & Smith, G. S. (1994). *Neutron reflectometry as optical imaging*. *J. Neutron Res.* **2**, 1–19.

Holy, V., Kubena, J., Ohlidal, I., Lischka, K. & Plotz, W. (1993). *X-ray reflection from rough layered systems*. *Phys. Rev. B*, **47**, 15896–15903.

Majkrzak, C. F. (1991). *Polarized neutron reflectometry*. *Physica (Utrecht)*, B**173**, 75–88.

Majkrzak, C. F., Ankner, J. F., Berk, N. F. & Gibbs, D. (1994) *Magnetic multilayers*, edited by L. H. Bennett & R. E. Watson, pp. 299–354. Singapore: World Scientific.

Merzbacher, E. (1970). *Quantum mechanics*, 2nd ed. New York: John Wiley.